Why some neutron stars become magnetars: chiral anomalies in the absence of magnetic helicity

Clara Dehman[1]*
[1] *Departament de Física, Universitat d'Alacant, 03690 Alicante, Spain*

The chiral magnetic effect (CME), arising from the chiral anomaly and enabling mutual conversion between magnetic helicity and electron chiral asymmetry, is a promising mechanism for generating large-scale magnetic fields in magnetars, key to explaining their observed slow spin-down within the first few decades after neutron star formation. Previous work by [1] demonstrated the CME's efficiency in the presence of an initially helical magnetic field, where magnetic helicity acts as a persistent internal source of chiral asymmetry, mediating energy transfer across scales and enabling the formation of large-scale dipolar fields ($B_{\rm dip} \gtrsim 10^{14}$, G) from small-scale fields expected at birth, without external energy input. However, the existence of helical fields at birth remains uncertain. Here, we systematically investigate the CME under varying helicity distributions, including cases with vanishing net helicity, to assess its role in neutron-star magnetic evolution. We find that dipolar field growth is closely linked to local chiral asymmetry, with the maximum chiral chemical potential ($\mu_5^{\rm max}$) controlling large-scale amplification. Our results show that any sufficiently strong, small-scale dominated field with magnetar-level strength, having spatial scales small enough for the CME to outpace Ohmic dissipation and containing localized regions of magnetic helicity, can drive efficient dipolar field amplification. This work extends the CME paradigm to realistic configurations, shedding light on early neutron-star magneto-thermal evolution and magnetar dipole formation.

I. INTRODUCTION

The transport of electric charge driven by quantum anomalies in chiral fermion systems has recently become a focal point of interest, particularly in the study of neutron stars and magnetars. This surge of attention reflects the possibility of accessing a distinct class of macroscopic quantum behavior. Conventional macroscopic quantum phenomena—such as superfluidity and superconductivity—emerge through symmetry breaking and are described by a local order parameter, for instance the Cooper-pair density [2]. By contrast, the anomaly-induced effects that arise in chiral systems are rooted in different physics and do not rely on symmetry breaking.

One of the most striking examples is the chiral magnetic effect (CME), where a chirality imbalance among charged fermions produces an electric current aligned with an external magnetic field $\boldsymbol{B}$ through the Adler–Bell–Jackiw anomaly [3, 4]. In this scenario, this mechanism operates in systems that remain in the normal phase, without any broken symmetries. Instead, the required chirality imbalance is connected, through the Atiyah–Singer index theorem [5], to the global topological structure of the gauge field. Because such topology is inaccessible to local diagnostics, the system lacks a local order parameter and is instead governed by topological order. Because the CME current acts as a source term in Maxwell's equations, a current flowing along the magnetic field twists the magnetic flux, generating nonzero magnetic helicity. Importantly, the coupling is reciprocal: a helicity-rich magnetic field can generate chiral asymmetry as it relaxes and untwists [6]. The validity of this mechanism has been confirmed in the context of neutron stars through 3D magneto-thermal simulations [1]. In particular, Dehman and Pons [1] demonstrated that a helical magnetic field[1] can sustain a chiral asymmetry between left- and right-handed electrons, enabling an inverse transfer of magnetic energy toward large scales and producing magnetar-strength dipolar components over a few decades. This direction of the coupling is especially significant for long-lived neutron stars, which are expected to be in chemical equilibrium at birth and therefore lack any initial chiral asymmetry to seed the magnetic field.

During the birth of a neutron star, MHD simulations indicate that the magnetic field is amplified by a turbulent dynamo during the proto-neutron star phase [7–13]. While these dynamos can generate magnetar-level total magnetic energy, most of it is stored in small-scale, non-axisymmetric, and toroidal components, leaving only a weak large-scale dipole. Long-term magneto-thermal evolution studies confirm that such configurations cannot account for observed magnetar properties when only Ohmic dissipation and Hall drift are considered in the evolution of the magnetic field within the neutron star interior [14, 15], although they may be relevant for other isolated neutron stars, such as Central Compact Objects or low-field magnetars. By contrast, the magnetic helicity content and its spatial distribution at neutron-star birth remain largely unexplored, yet they may critically influence whether the CME can drive the transfer of magnetic energy from small to large scales. It is currently unknown whether the magnetic field at birth carries a net helicity, and theoretical arguments exist supporting

* clara.dehman@ua.es

[1] A magnetic field configuration with net magnetic helicity.

both possibilities. One scenario leading to net magnetic helicity arises if the CME operates during core-collapse supernovae: the chiral asymmetry present at that stage is gradually erased as the system relaxes toward chemical equilibrium in the newly formed neutron star, generating net magnetic helicity through the chiral anomaly [12]. By contrast, standard MHD simulations preserve reflectional symmetry, so that an initially vanishing helicity leads to the development of mirror-image structures with opposite handedness [16–18], allowing magnetic energy to grow while the net helicity remains negligible [19]. Motivated by these uncertainties, we explore a range of plausible magnetic configurations representative of newborn neutron stars, systematically varying both the initial helicity content and its spatial distribution. Our goal is to identify which configurations can evolve into stable, large-scale dipolar fields characteristic of magnetars, and to assess whether a non-helical initial magnetic field can also effectively trigger the chiral magnetic effect.

The structure of the paper is as follows. Section II introduces the theoretical framework employed in this work. Section III details the numerical setup and initial conditions. The results are presented in Section IV and discussed in Section V.

II. MAGNETIC FIELD FORMALISM

Magnetic helicity is a fundamental topological invariant, expressible in terms of the Chern–Simons three-form, and provides a quantitative measure of the twist, writhe, and linkage of magnetic-field lines [20–23]. It remains nearly conserved even in non-ideal, high–magnetic-Reynolds-number regimes, as demonstrated in studies of magnetic reconnection in the solar atmosphere [24], and is increasingly recognized as a key factor in neutron-star magnetic evolution [25, 26]. Magnetic helicity is defined as

$$\chi_M = \int_V \boldsymbol{A}\cdot\boldsymbol{B}\,dV \tag{1}$$

where $\boldsymbol{A}$ is the magnetic vector potential, $\boldsymbol{B}=\boldsymbol{\nabla}\times\boldsymbol{A}$ is the magnetic field, and V denotes the integration volume.

The time evolution of χ_M is given by [27]

$$\frac{\partial(\boldsymbol{A}\cdot\boldsymbol{B})}{\partial t} = -2c\boldsymbol{E}\cdot\boldsymbol{B} - c\boldsymbol{\nabla}\cdot(\boldsymbol{E}\times\boldsymbol{A}), \tag{2}$$

where c is the speed of light and $\boldsymbol{E}$ the electric field. The term $\propto(\boldsymbol{E}\times\boldsymbol{A})$ represents the helicity flux across the boundary, whose contribution is negligible.

Helicity conservation acquires additional significance when quantum anomalies are taken into account [28]. Through the chiral anomaly, magnetic helicity couples directly to fermionic chirality, altering $n_L - n_R$. The evolution of the chiral number density, $n_5 \equiv n_R - n_L$, is given by [1, 3, 29]:

$$\frac{\partial n_5}{\partial t} = \frac{2\alpha}{\pi\hbar}\boldsymbol{E}\cdot\boldsymbol{B} - n_5\Gamma_f. \tag{3}$$

This relation includes both source and sink terms. The $\boldsymbol{E}\cdot\boldsymbol{B}$ term governs the coupling between chiral density and the electromagnetic field: twisting or untwisting magnetic field lines changes electron chirality, acting as a source or a sink depending on its sign. The reaction rate Γ_f accounts for spin-flip interactions due to electromagnetic effects and the finite electron mass; it always acts as a sink, reducing the efficiency of the CME and suppressing the chiral magnetic instability (CMI) [29–32]. The magnitude of the spin-flip rate casts significant doubt on the relevance of the CME in short-lived environments such as PNSs. Nonetheless, the first study of long-lived NSs [1] demonstrated that chiral asymmetries can persist for centuries in the presence of small-scale, tangled magnetic structures, enabling a sustained transfer of magnetic energy from small to large scales despite the strong suppressive effect of spin-flip processes. For a simplified framework describing how the chiral anomaly operates, please refer to Section II B.

Eq. (2) and Eq. (3), when combined and integrated over the volume, yield a generalized helicity balance law [1, 6, 28, 33]:

$$\frac{d}{dt}\left(Q_5 + \frac{\alpha}{\pi\hbar c}\chi_m\right) + \Gamma_5 = 0, \tag{4}$$

where $Q_5 = \int n_5\,dV$ is the total axial charge, quantifying the global imbalance between left- and right-handed fermions, and $\Gamma_5 = \int n_5\,\Gamma_f\,dV$ is the total spin-flip dissipation rate. The appearance of the sink term Γ_5 indicates that total helicity is not strictly conserved.

A local imbalance between left- and right-handed electrons induces an electric current parallel to the magnetic field through the Adler–Bell–Jackiw anomaly [3, 4], adding an extra term to Maxwell's equations [34]:

$$\boldsymbol{J}_5 = \frac{\alpha\mu_5}{\pi\hbar}\boldsymbol{B}, \tag{5}$$

where $\mu_5 \equiv \mu_R - \mu_L$ is the chiral chemical potential, $\alpha = e^2/(\hbar c)$ the fine-structure constant, e the elementary charge, $\hbar$ the reduced Planck constant. Gaussian units are used throughout this section.

In this work, we focus on the CME in the neutron star crust, where the spin-flip rate is given by $\Gamma_f = 4\alpha/(3\pi\sigma_e)$. This focus is motivated by our previous results showing that the CME can operate efficiently in the crust despite the presence of spin-flip processes [1]. In contrast, the neutron star core—which comprises the majority of the stellar volume—is characterized by much more rapid spin-flip damping, primarily due to electron scattering off magnetized neutron vortices in the superfluid [35, 36]. These processes occur on significantly shorter timescales than in the crust and are therefore expected to strongly suppress any chiral asymmetry. As a result, it remains unclear whether a residual asymmetry could survive long enough to influence magnetic field evolution in the core, a question that merits further investigation in future work.

The modified induction equation in the neutron star crust, incorporating Ohmic dissipation, Hall drift, and the chiral magnetic contribution, is given by [1]:

$$\frac{\partial \boldsymbol{B}}{\partial t} = -\boldsymbol{\nabla} \times \left[\eta \left(\boldsymbol{\nabla} \times \boldsymbol{B} - k_5 \boldsymbol{B}\right) + f_h \left(\boldsymbol{\nabla} \times \boldsymbol{B}\right) \times \boldsymbol{B}\right]. \quad (6)$$

The first term on the right-hand side represents Ohmic dissipation, where the magnetic diffusivity is defined as $\eta \equiv c^2/(4\pi\sigma_e)$. This term leads to the decay of the magnetic field and is most effective at small spatial scales. The second term corresponds to the CME, with the chiral wavenumber defined as $k_5 = 4\alpha\mu_5/(\hbar c)$. This term can drive exponential growth of certain magnetic field modes by transferring energy from others. The last term represents the Hall drift, where $f_h = c/4\pi e n_e$ is the Hall prefactor. Here, σ_e denotes the electron conductivity and n_e the electron number density. The Hall drift is known to generate a direct cascade, transferring magnetic energy from large-scale structures to smaller scales, where it is more efficiently dissipated by Ohmic diffusion [14, 37]. In addition, in the presence of helical (or partially helical) magnetic fields, the Hall term can also drive an inverse cascade. In this regime, the approximate conservation of magnetic helicity implies that, as magnetic energy is dissipated, the characteristic wavenumber shifts toward smaller values, corresponding to larger spatial scales. Consequently, the inverse cascade proceeds on the magnetic dissipation timescale [25, 26]. However, as shown in Dehman and Brandenburg [26], the extent of the inverse cascade is limited by the inverse aspect ratio of the neutron star crust, $\mathcal{A} \approx 1/30$. For a comprehensive overview of magneto-thermal evolution in neutron stars, we refer the reader to the recent review by Pons, Dehman, and Viganò [38].

A. Quasi-equilibrium and astrophysical timescales

When spin-flip reactions are included, their rates are extremely large—of order $10^{15} - 10^{17}$ s^{-1} under typical neutron-star conditions during the first few centuries. Because these rates exceed macroscopic magnetic-evolution timescales by many orders of magnitude, the system remains in a quasi-equilibrium state [see Section II of Ref. 1]. In this regime—effectively always realized in astrophysical contexts—one can derive an explicit expression for k_5 as a function of the magnetic field:

$$k_5\left(\boldsymbol{x}, t\right) = \frac{\left(\boldsymbol{\nabla} \times \boldsymbol{B}\right) \cdot \boldsymbol{B}}{\left(\dfrac{2\mu_e^2}{m_e^2 c^4}\right) \dfrac{B_{\rm QED}^2}{3\pi} + B^2}\,, \quad (7)$$

where $B_{\rm QED} \equiv m_e^2 c^3/(e\,\hbar) = 4.41 \times 10^{13}$ G is the Schwinger critical field. This expression shows that the chiral wavenumber k_5 is locally constrained by the characteristic wavenumber of the current aligned with the magnetic field. It also demonstrates that the CME operates efficiently only in the strong-field regime ($B \gtrsim B_{\rm QED}$), as found in magnetars—a conclusion that emerges naturally once spin-flip processes, typically neglected in CME studies, are properly accounted for.

Neglecting the helicity flux across the boundaries, which is negligible in this context, Eq. (2) can be rewritten as

$$\frac{\partial(\boldsymbol{A} \cdot \boldsymbol{B})}{\partial t} = -2\,\eta\,\left(\boldsymbol{\nabla} \times \boldsymbol{B}\right) \cdot \boldsymbol{B} \left(\frac{1}{1 + \dfrac{B^2}{B_{sat}^2}}\right), \quad (8)$$

where $B_{\rm sat}$ is the characteristic magnetic field strength at which saturation sets in, given by

$$B_{\rm sat} \approx \sqrt{\frac{2}{3\pi}} \frac{\mu_e}{m_e c^2} B_{\rm QED}. \quad (9)$$

It scales linearly with the ratio $\mu_e/(m_e c^2)$, which increases with density, giving $B_{\rm sat} \sim 10^{14}$ G near the surface and up to $\sim 5 \times 10^{15}$ G in deeper layers—consistent with inferred magnetar field strengths.

In the quasi-equilibrium limit, Eq. (8) establishes a direct connection between the evolution of the local magnetic–helicity density and the local current–helicity density, modulated by the magnetic diffusivity. Consequently, the sign (and magnitude) of $(\boldsymbol{\nabla} \times \boldsymbol{B}) \cdot \boldsymbol{B}$—which reflects the local alignment, anti-alignment, or near-orthogonality of the electric current with the magnetic field—determines whether helicity is generated, dissipated, or remains largely unaffected. The efficiency of this helicity transfer, and thus the effectiveness of the CME (see Eq. (4)), varies strongly with radius due to the steep radial gradient in magnetic diffusivity. In regions with higher diffusivity, such as the outer crust and the nuclear pasta layer, magnetic structures relax more rapidly, facilitating a more effective conversion between magnetic helicity and chiral asymmetry. To quantify this process, we define

$$\varpi = \eta\,\left(\boldsymbol{\nabla} \times \boldsymbol{B}\right) \cdot \boldsymbol{B}, \quad (10)$$

which will be evaluated in our study.

B. A simplified framework for the chiral anomaly

In ultra-strong magnetic fields exceeding the Schwinger QED critical value, $B_{\rm QED} \equiv m_e^2 c^3/(e\,\hbar) = 4.41 \times 10^{13}$ G, as expected in magnetar interiors, the motion of electrons perpendicular to the magnetic field is quantized into Landau levels such that only the lowest Landau level (LLL) is populated [39, 40]. Consequently, the transverse degrees of freedom are frozen, and in the LLL the electron spins anti-align with the magnetic field to minimize their energy, allowing electrons to propagate only along the field direction [41, 42]. If $\boldsymbol{B}$ points along the x-direction, negatively charged left-handed fermions (i.e., left-handed electrons) propagate in the positive x-direction, while

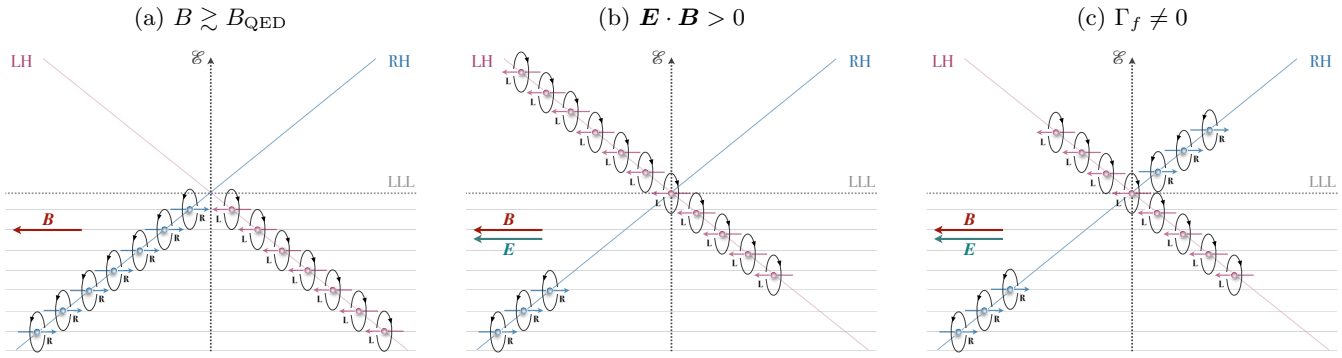

FIG. 1: Illustration of the chiral anomaly in a very strong magnetic field, $B \gtrsim B_{\rm QED}$, pointing in the $\hat{\boldsymbol{x}}$-direction. The momenta of right-handed electrons are shown in blue, while the momenta of left-handed electrons are shown in pink. *Panel (a):* Due to the very strong magnetic field, all electrons occupy the LLL and can move only along the direction of the magnetic field. The momenta of right-handed electrons point opposite to the magnetic field, whereas the momenta of left-handed electrons point in the same direction as the magnetic field. Initially, there are equal numbers of left-handed and right-handed electrons. *Panel (b):* As the magnetic helicity relaxes, an electric field is induced, resulting in a non-vanishing $\boldsymbol{E}\cdot\boldsymbol{B}$. Assuming $\boldsymbol{E}\cdot\boldsymbol{B} > 0$, a right-handed electron is converted into a left-handed electron by reversing the direction of its momentum. The left-handed electron then moves upward. *Panel (c):* Once electrons leave the LLL, they can flip chirality, thereby significantly reducing the chiral asymmetry. Note that these processes occur on very short time scales and effectively take place simultaneously.

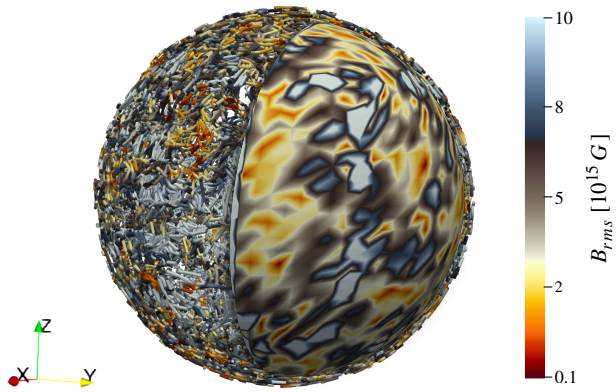

FIG. 2: Schematic representation of the initial magnetic field configurations.

negatively charged right-handed fermions propagate in the negative x-direction [43].

This effect is illustrated in panel (a) of Fig. 1, where the magnetic field is assumed to be uniform and oriented along the x-direction, i.e., $\boldsymbol{B} = B_z\hat{\boldsymbol{x}}$. Initially, equal numbers of left-handed and right-handed electrons are present, corresponding to neutron-star matter in chemical equilibrium, with no net chiral asymmetry.

Assuming the initial magnetic field is helical, as the field lines untwist, the magnetic helicity decreases slightly due to finite magnetic diffusivity, inducing a nonzero $\boldsymbol{E}\cdot\boldsymbol{B}$ term. In this case, some of the electrons change their helicity. Since spin flips are energetically suppressed in a strong magnetic field, helicity can only change through a reversal of the electron momentum. For $\boldsymbol{E}\cdot\boldsymbol{B} > 0$, the induced electric field is locally aligned with the magnetic field: left-handed electrons moving along the field propagate upward, while right-handed electrons are converted into left-handed electrons by reversing their momenta [43]. Although the total number of electrons, $N_e = N_R + N_L$, is conserved, the axial charge, $N_5 = N_R - N_L$, is not, resulting in an electromagnetic current, $\boldsymbol{J}_5$, along the direction of $\boldsymbol{B}$ that reflects the presence of the axial (chiral) anomaly. In this scenario, the evolution of the magnetic field couples primarily to the left-handed current, $\mathbf{J}_5 \simeq \mathbf{J}_L$. This mechanism is illustrated in panel (b) of Fig. 1.

Conversely, if the electric field is anti-aligned with the magnetic field ($\boldsymbol{E}\cdot\boldsymbol{B} < 0$), right-handed electrons in the LLL propagate upward, whereas left-handed electrons are converted into right-handed electrons by reversing their momenta, and the magnetic-field evolution couples primarily to the right-handed current, $\boldsymbol{J}_5 \simeq \boldsymbol{J}_R$.

In addition to the anomalous generation of axial charge by a non-vanishing $\boldsymbol{E}\cdot\boldsymbol{B}$, chirality-flipping processes act to relax the resulting imbalance [30]. In the ultra-strong magnetic-field regime, where electrons predominantly occupy the LLL, a genuine spin-flip interaction cannot occur within the LLL, which admits only a single spin polarization [42]. Such processes therefore become effective only when electrons are excited to higher Landau levels, where spin and momentum are no longer rigidly locked and chirality is not conserved [44]. Finite electron-mass effects and electromagnetic scattering interactions then convert right- and left-handed electrons into one another,

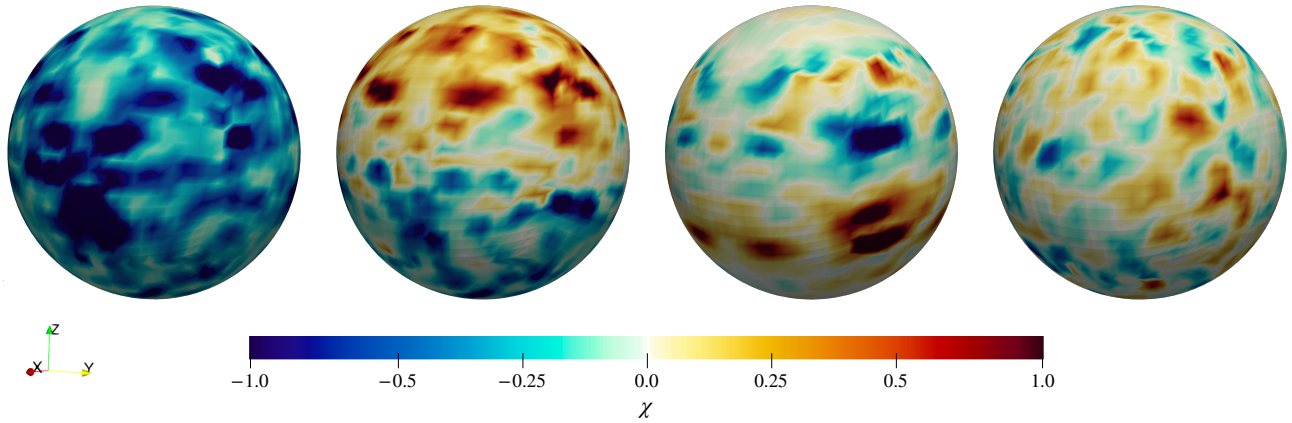

FIG. 3: Schematic representation of χ, the local helicity, normalized by its maximum value, for the `Monohel`, `Bihel`, `Mixhel`, and `Angfluc` setups.

leading to a relaxation of the axial charge N_5. The role of these chirality-flipping processes is illustrated in panel (c) of Fig. 1. Note that these processes occur on very short timescales, effectively simultaneously, and locally within the interior of a neutron star.

III. NUMERICAL SETUP

To study the magnetic field evolution under the CME, we use the extended `MATINS` code introduced in Dehman and Pons [1], which, in addition to solving the coupled induction and heat-diffusion equations, self-consistently incorporates the evolution of chiral number density and spin-flip contributions arising from the chiral anomaly. This extension builds on the earlier version of `MATINS`[2] described in Dehman *et al.* [14, 45], Ascenzi *et al.* [46], which did not include the CME.

We model the entire neutron star volume while limiting the magnetic field evolution to the crust by imposing potential-field (current-free) boundary conditions at the mass density $\rho = 10^{10}\,\mathrm{g\,cm^{-3}}$, which defines the numerical surface of the star, and perfect-conductor conditions at the crust–core interface, thereby confining the magnetic field to the crust (see Dehman *et al.* [45] for details on the magnetic boundary conditions). The temperature-dependent electrical conductivity is computed using the IOFFE codes[3] [47]. The stellar background in `MATINS` is constructed using zero-temperature EOSs from the CompOSE[4] database. In this work, we adopt the BSk24 [48] EOS and consider a canonical $1.4\,M_\odot$ star, yielding $R = 12.4$ km and a crust thickness of 0.86 km, although `MATINS` allows exploration of other EOSs and stellar masses.

[2] https://github.com/ice-csic-astroexotic/MATINS
[3] http://www.ioffe.ru/astro/conduct/
[4] https://compose.obspm.fr/

The magnetic field configuration of neutron stars at birth remains poorly constrained, and consequently, both its magnetic-helicity content and spatial distribution are largely unknown. During the proto-neutron star stage, dynamo processes are expected to drive the system toward a quasi-equilibrium state, in which magnetic energy is distributed across a broad range of spatial scales. This configuration is typically dominated by non-axisymmetric and toroidal components, with only a weak large-scale dipole [7–10, 13, 49]. While the total magnetic energy can reach magnetar-like levels, it is concentrated on small spatial scales.

Rather than attempting to model the full diversity of magnetic-field configurations predicted by proto-neutron-star studies, we initialize the system with a magnetic field whose energy is concentrated at small spatial scales and whose spectrum peaks at a characteristic angular wavenumber ℓ_0. In the sub-inertial range ($\ell < \ell_0$), we adopt a spectrum corresponding to a random vector potential. In three dimensions, this implies a vector potential spectrum $E_A(\ell) \propto \ell^2$ and a magnetic energy spectrum $E_M(\ell) \propto \ell^4$ (see Table 1 of Dehman and Brandenburg [26]). This form, commonly used in cosmology and referred to as a causal spectrum [50], describes a divergence-free field with no spatial correlations beyond the generation scale. The magnetic energy spectrum peaks at $\ell_0 \simeq 50$ and extends up to $\ell_{\max} = 70$. For the radial wavenumber k_r, we adopt values of order a few hundred, chosen to balance the fastest-growing mode of the CMI against Ohmic dissipation (see Appendix II of Dehman and Pons [1]). The radial direction is resolved more finely than the angular directions for both physical and numerical reasons. Physically, the CME is sensitive to neutron-star microphysics, which exhibits strong radial gradients. Numerically, `MATINS` is not parallelized, and the spherical harmonic decomposition required for higher angular resolution is computationally more demanding. Accordingly, the crust is discretized with 200 radial grid points, allowing structures down to

TABLE I: Simulation data at representative times, showing the magnetic field strength, the chiral chemical potential (mean and maximum), and the fractional magnetic helicity.

Run	$B_{\rm rms}$ [G]		$B_{\rm dip}$ [G]		$\mu_5^{\rm avg}$ [MeV]		$\mu_5^{\rm max}$ [MeV]		$\tilde{\chi}$
	$t=0$	$t=100$	$t=0$	$t=100$	$t=0$	$t=100$	$t=0$	$t=100$	$t=0$
`Monohel`	2.9×10^{16}	2.3×10^{16}	4.3×10^{12}	1.0×10^{14}	2×10^{-12}	1×10^{-12}	2×10^{-11}	1×10^{-11}	0.853
`Bihel`	3.0×10^{16}	2.0×10^{16}	4.1×10^{12}	1.6×10^{14}	-5×10^{-14}	-5×10^{-14}	8×10^{-11}	2×10^{-11}	0.031
`Mixhel`	2.9×10^{16}	1.5×10^{16}	3.9×10^{12}	1.1×10^{14}	-2×10^{-13}	-1×10^{-13}	1×10^{-10}	1×10^{-11}	0.130
`Angfluc`	2.8×10^{16}	1.5×10^{16}	4.3×10^{12}	1.5×10^{14}	9×10^{-15}	2×10^{-14}	1×10^{-10}	2×10^{-11}	0.007
`Radfluc`	2.8×10^{16}	1.3×10^{16}	4.0×10^{12}	1.1×10^{14}	-3×10^{-15}	-2×10^{-15}	9×10^{-11}	2×10^{-11}	0.001
`NoCME`	3.0×10^{16}	1.0×10^{15}	4.0×10^{12}	1.3×10^{11}	0.0	0.0	0.0	0.0	0.031

scales of tens of meters to be resolved. The angular directions are discretized using a cubed-sphere grid [45] with $N_\xi = N_\eta = 47$ points per patch over six patches, corresponding to effective resolutions of $N_\theta = 94$ and $N_\varphi = 188$, and resolving angular scales of several hundred meters.

With this numerical setup, the initial magnetic field has a characteristic strength of order 10^{16} G, predominantly concentrated at small scales and close to equipartition between poloidal and toroidal components, with a slight dominance of the toroidal component. The large-scale dipolar field is limited to $\sim 10^{12}$ G, yielding a total magnetic energy of $\sim 10^{49}$ erg, consistent with expectations for neutron-star birth [10, 11]. An example of such an initial configuration is shown in Fig. 2, where the color scale indicates the magnetic field strength.

Since the magnetic helicity at neutron-star birth remains largely unexplored, we vary its initial content and spatial distribution, considering several setups that span plausible configurations for a newborn neutron star. This allows us to assess whether a non-helical initial magnetic field can drive magnetic energy transfer across scales and lead to large-scale field formation. The helicity distributions considered in this study are listed below:

(i) `Monohel` – a helical configuration with a uniform helicity sign throughout the neutron-star crust;

(ii) `Bihel` – a bi-helical configuration with opposite helicity signs in the northern and southern hemispheres, yielding an approximately vanishing net helicity;

(iii) `Mixhel` – a configuration with mixed helicity across the northern and southern hemispheres, yielding an approximately vanishing net helicity;

(iv) `Angfluc` – a configuration with small-scale, localized helicity fluctuations in the angular directions, leading to an approximately vanishing net helicity;

(v) `Radfluc` – a configuration with small-scale, localized helicity fluctuations in the radial direction, also yielding an approximately vanishing net helicity, in which different radial functions for the poloidal and toroidal components were used (see Appendix A and Fig. 8);

(vi) `NoCME` – identical to the `Bihel` setup but with the *CME* deactivated, serving as a reference case.

Details on the construction of each configuration are provided in Appendix A, and the key parameters are summarized in Table I. The local 3D distribution of the initial magnetic helicity, normalized by its maximum absolute value, $\chi(r,\xi,\eta,t) = \boldsymbol{A}\cdot\boldsymbol{B}/\left|\boldsymbol{A}\cdot\boldsymbol{B}\right|_{\rm max}$, is shown in Fig. 3 for the Helical, Bi-helical, Random, and Mixed runs, respectively. For the Fluctuation run, see Fig. 8. This normalized helicity represents the local helicity relative to its maximum absolute value, highlighting the spatial distribution of positive and negative helicity regions and allowing comparison of patterns across simulations without implying a global net helicity.

Each setup is evolved in full neutron-star crust simulations over the first thousand years using day-long timesteps. We focus on these early evolutionary stages to assess whether the CME can drive the formation of the youngest known magnetars, such as Swift J1818.0–1607 (~ 200 yr; 51), on such short timescales. To isolate the effects of the CME from those of the Hall drift—which also redistributes magnetic energy across spatial scales—we switch off the Hall term in the present study. The implications of Hall effects are discussed at the end of Section IV.

IV. RESULTS

The time evolution of the fractional magnetic helicity, defined as

$$\tilde{\chi} = \sqrt{\langle \boldsymbol{A}\cdot\boldsymbol{B}\rangle\langle \boldsymbol{J}\cdot\boldsymbol{B}\rangle}\,/\,\langle \boldsymbol{B}^2\rangle, \tag{11}$$

is shown in Fig. 4 (solid lines). The quantity $\tilde{\chi}$ was introduced by Brandenburg [25] and provides a more rigorous measure of the degree of helicity of the magnetic field. The dashed lines correspond to the normalized losses due to the spin-flip term for each run. The different simulation runs are distinguished by markers, as indicated in the figure caption.

The fractional magnetic helicity, denoted by $\tilde{\chi}$, is equal to unity for a fully helical Beltrami field with periodic boundary conditions [25]. For non-periodic boundary conditions—such as perfectly conducting on one side and

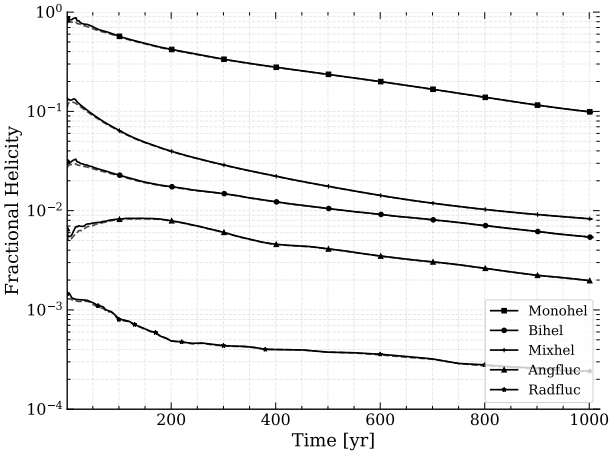

FIG. 4: Time evolution of the fractional magnetic helicity (solid lines) and the normalized losses due to the spin-flip term (dashed lines). Simulation runs are distinguished by markers: squares (`Monohel`), circles (`Bihel`), plus symbols (`Mixhel`), triangles (`Angfluc`), and stars (`Radfluc`).

a potential field condition on the other—$\tilde{\chi}$ can still be close to unity, as is the case for the `Monohel` run, with $\tilde{\chi}(t_0) \approx 0.85$ (see also Table.I). In general, the closer $\tilde{\chi}$ is to unity, the more helical the field; conversely, values close to zero correspond to non-helical fields with vanishing magnetic helicity.

The other runs start with much lower values of fractional magnetic helicity, with `Mixhel` has $\tilde{\chi}(t=0) \approx 0.1$. This is followed by `Bihel`, where magnetic helicity cancels more efficiently between positive and negative local contributions, yielding $\tilde{\chi}(t=0) \approx 0.03$. These values indicate that both runs can be considered effectively non-helical. Finally, the `Angfluc` and `Radfluc` runs exhibit $\tilde{\chi} \ll 1$.

Figure 4 shows the impact of the generalized helicity (Eq. (4)). The left panel shows the time evolution of three quantities: the total helicity $Q_5 + \frac{\alpha}{\pi \hbar c}\chi_m$ (dashed blue); the losses due to the spin-flip term at each time step $-\Gamma_5 \Delta t$ (dash-dotted orange), representing the number of right-handed electrons flipping to left-handed ones in the entire crust during one time step; and Q_5 itself (dotted teal), which reflects the total excess of right-handed electrons. The figure illustrates how the magnetic helicity generates an extremely small Q_5 (20 orders of magnitude smaller), which remains nearly constant. This is due to the strong damping effect of the spin-flip term. In the absence of spin-flip processes, Q_5 would grow until it is of the order of the magnetic helicity. Moreover, the figure confirms that our simulations respect the generalized helicity conservation law (Eq. (4)): the change in total helicity is closely balanced by the spin-flip term, as predicted by theory. Nonetheless, helicity is conserved to a satisfactory degree for the purposes of this analysis and it decay over time due to the magnetic diffusivity.

A. Magnetic energy and helicity Spectra

To assess the impact of the chiral asymmetry on the evolution of the magnetic field, we examine the magnetic helicity spectra defined as

$$\chi_M(\ell, m; t) = 2 \int \ell(\ell+1)\Phi_{\ell m}\Psi_{\ell m} dr, \tag{12}$$

and the magnetic energy spectrum defined as

$$E_{\rm M}(\ell, m; t) = \frac{1}{2}\int \frac{\ell(\ell+1)}{r^2}\left[\frac{\ell(\ell+1)}{r^2}\Phi_{\ell m}^2 + {\Phi'_{\ell m}}^2 + \Psi_{\ell m}^2\right], \tag{13}$$

where, $\Phi'_{\ell m} = \partial\Phi_{\ell m}/\partial r$. These quantities are evaluated for the five runs introduced in Section III. The left panels of Fig. 5 show the magnetic helicity spectrum $\chi_M(\ell, t)$ as a function of spherical harmonic degree ℓ (horizontal axis) and time (vertical axis), with color indicating its magnitude. The right panels show the magnetic energy spectrum $E_M(\ell)$ as a function of ℓ at different simulation times, with color representing time. We examine the evolution of the system over the first 10^3 yr of the magnetar lifetime.

Initially, the magnetic helicity $\chi_M(\ell, t=0)$ can take both positive and negative values, reaching its largest magnitudes at small spatial scales, predominantly in the range $10 \lesssim \ell \lesssim 55$, depending on the run. In contrast, the large-scale structures are essentially non-helical in all simulations. Similarly, the smallest resolved scales, corresponding to $60 \lesssim \ell \lesssim 70$, also exhibit negligible helicity. At $t = 0$, the magnetic energy is likewise concentrated at small scales, with only weak contributions at large scales. In particular, the initial magnetic energy spectrum follows $E_M(\ell) \propto \ell^4$, indicating that most of the magnetic energy resides at high spherical harmonic degrees.

As the system evolves, magnetic helicity is progressively transferred from the small spatial scales that initially contain most of it to other scales that initially possess negligible helicity, including both larger and smaller scales. The total magnetic helicity remains approximately conserved throughout the evolution, exhibiting only a slow decay with time (see also Fig. 5 of Dehman and Pons [1]). This qualitative behavior is observed in all the simulations considered here.

The rate at which magnetic helicity is redistributed across multipoles varies between the simulations, with this variation being particularly pronounced in the `Monohel` run (upper-left panel) compared to the other cases. In the `Monohel` simulation, the dipolar component ($\ell = 1$) requires nearly 100 yr before a significant fraction of helicity is transferred, whereas in the other simulations this redistribution occurs much more rapidly, typically within one to two decades. This helicity redistribution is accompanied by a concurrent transfer of magnetic energy across multipoles, preferentially channeling energy from strongly tangled, highly helical structures toward modes with lower helicity content. In the `Monohel` run, the transfer of magnetic energy proceeds

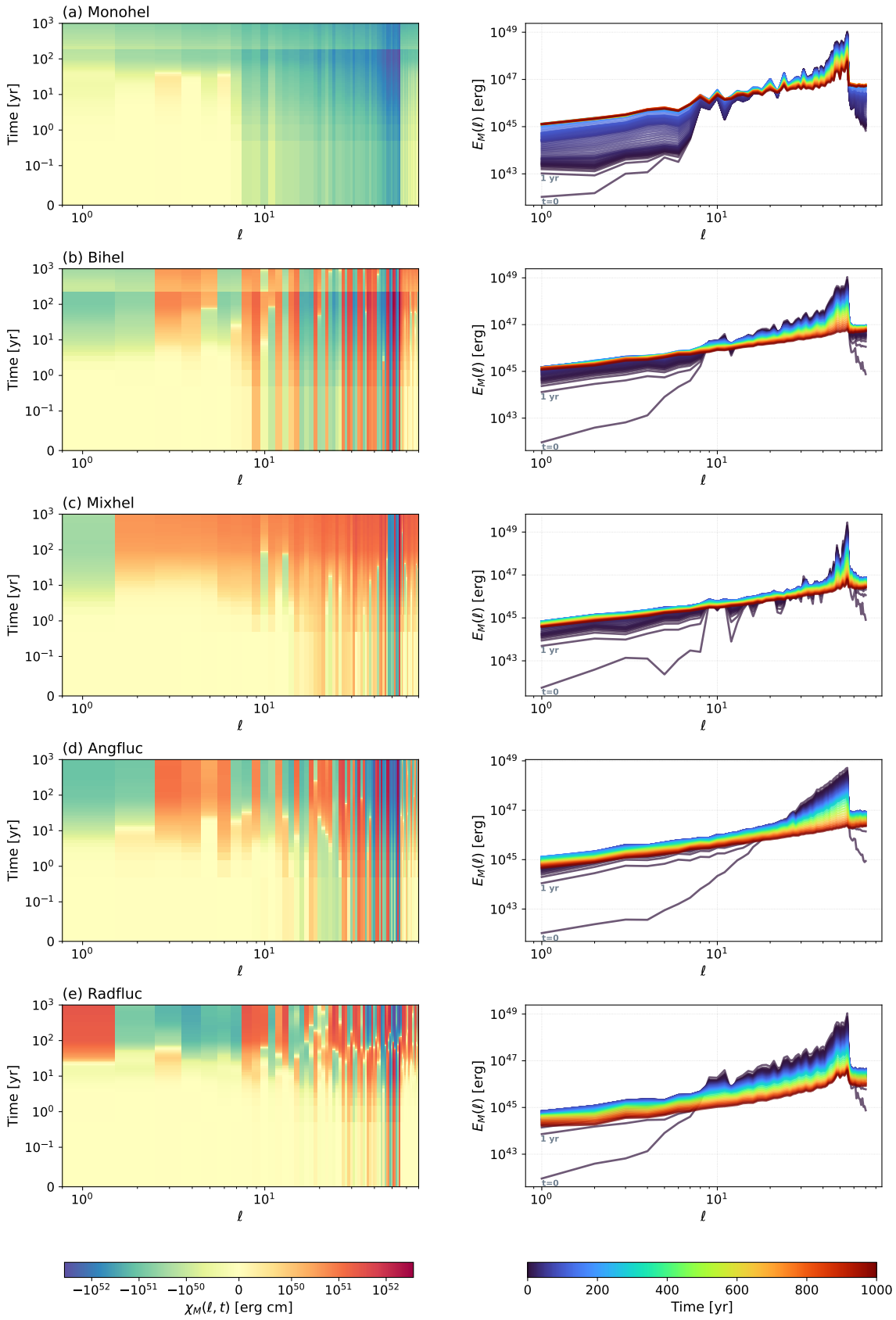

FIG. 5: Magnetic helicity and magnetic energy spectra for the five simulations: (a) `Monohel`, (b) `Biohel`, (c) `Mixhel`, (d) `Angfluc`, and (e) `Radfluc`. The left column shows the magnetic helicity spectrum $\chi_M(\ell, t)$ as a function of spherical harmonic degree ℓ (horizontal axis) and time (vertical axis), with the color indicating the helicity amplitude. The right column shows the magnetic energy spectrum $E_M(\ell)$ as a function of ℓ at different times, with the color encoding the simulation time. The corresponding colorbars are shown below each column.

more slowly than in any other simulation, a difference that is evident in the right-hand panel, where, after one year, energy transfer in the other simulations is already markedly more efficient, as indicated by the pronounced change in the slope of the energy spectra.

As the system evolves, the slope of the magnetic energy spectrum gradually approaches an approximately linear dependence on ℓ, giving rise to an inverse-like cascade. This process differs from the standard MHD inverse cascade, which is characterized by a shift of the spectral peak toward lower ℓ while approximately conserving the initial slope of the spectrum (see also Brandenburg 25, Dehman and Brandenburg 26 for studies of the inverse cascade under the non-linear Hall term in neutron stars). Despite this redistribution, small-scale structures remain dominant in the magnetic field configuration, a behavior that is consistent across all simulations considered here and suggests that each multipole saturates at its own characteristic amplitude.

Note that at much later times, of the order of tens of kiloyears, this spectral behavior may change as Ohmic dissipation progressively removes the small-scale magnetic structures while leaving the dipolar component comparatively less affected. However, over such long evolutionary timescales the Hall term, which is not included in the present simulations, is also expected to play an important role. In particular, it can transfer magnetic energy from the already formed dipole back to smaller scales, eventually establishing what is known as a Hall balance [14]. Determining the resulting long-term spectral shape therefore requires models that include both Ohmic dissipation, chiral magnetic effect, and Hall dynamics.

A particularly notable feature of this evolution is the strong amplification of the dipolar component ($\ell = 1$; see right panels), reflecting the spontaneous formation of the largest spatial scale in the system. While similar behavior occurs for other large-scale structures ($\ell \lesssim 10$), we focus on the dipole due to its primary relevance for magnetars. This amplification is observed in all simulations; however, differences arise in the subsequent evolution of the dipole. In the `Monohel` and `Bihel` runs, the dipole, once established, remains stable over time, with energy dissipation occurring predominantly in the smaller-scale structures. By contrast, in the `Mixhel` run, the large-scale structures undergo slight dissipation during the first thousand years, driven not by Ohmic diffusion but by the CME acting to destabilize the formed dipolar field. This effect is more pronounced in `Angfluc` and becomes strongest in `Radfluc`. Importantly, this trend extends to the smallest scales generated by the CME ($\ell \gtrsim 55$), which exhibit a similar pattern of dissipation.

In `Monohel` and `Bihel` runs—those that produce the most stable dipoles—the helicity contained in the dipole first increases, then decreases, and later increases again. This behavior suggests an ongoing exchange of helicity between the dipole and other multipoles, allowing the dipole to be replenished and thereby maintained. By contrast, in the `Angfluc` and `Radfluc` runs, where the dipole eventually decays, the helicity stored in the dipole becomes comparatively large relative to that of the other multipoles. In this regime, the dipole appears to act as a source that feeds helicity into other modes through the CME, thereby destabilizing the large-scale field. The `Mixhel` case represents an intermediate regime in which the dipole does not accumulate enough helicity to significantly fuel other multipoles, resulting in a partially stable configuration.

The sign of the magnetic helicity also exhibits distinct behavior across the simulations. In the `Monohel` run, the helicity initially has a negative sign, resulting in a net magnetic helicity in the system. The magnetic helicity is approximately conserved throughout the evolution, which is consistent with the fact that the helicity associated with individual multipoles does not exhibit significant sign reversals. In contrast, the other simulations initially contain both positive and negative helicity contributions across different multipoles. This distribution yields an overall helicity that is close to zero and remains approximately balanced during the subsequent evolution. In these cases, individual multipoles can undergo substantial variations in their helicity amplitude and may even change sign.

Because the multipoles that initially carry magnetic helicity evolve in a non-uniform manner—some reversing their helicity sign more frequently than others—this behavior suggests that certain modes couple more efficiently to other multipoles, particularly those with initially negligible helicity. Quantifying these couplings requires a detailed spherical harmonic decomposition of the induction and helicity evolution equations, where the nonlinear interactions between modes are governed by Clebsch–Gordan coefficients.

B. Decay and instability laws

The time evolution of the volume-averaged magnetic field and its dipolar component is shown in Fig. 6 for the first 10^3 years of neutron star lifespan. The colorbar in the left panel indicates the evolution of $|\mu_5^{\rm avg}|$, while that in the right panel represents the temporal evolution of $|\mu_5^{\rm max}|$. Simulation runs are depicted by solid lines with distinct markers: squares denote `Monohel` run, circles correspond to `Bihel` configuration, plus symbols denote `Mixhel` run, triangles represent `Angfluc` case, stars indicate `Radfluc` run, and diamonds denote the `NoCME` run. For the latter, the evolution of the chiral chemical potential is not shown, as the CME is switched off in this simulation.

The time evolution of the volume-averaged magnetic field (left panel of Fig. 6) begins with nearly identical initial magnetic field strengths, $B_{\rm rms} \simeq 3 \times 10^{16}\,{\rm G}$, for all the simulations studied here and it then decreases over time. This behavior is expected, as we consider a decaying MHD scenario. In this framework, the

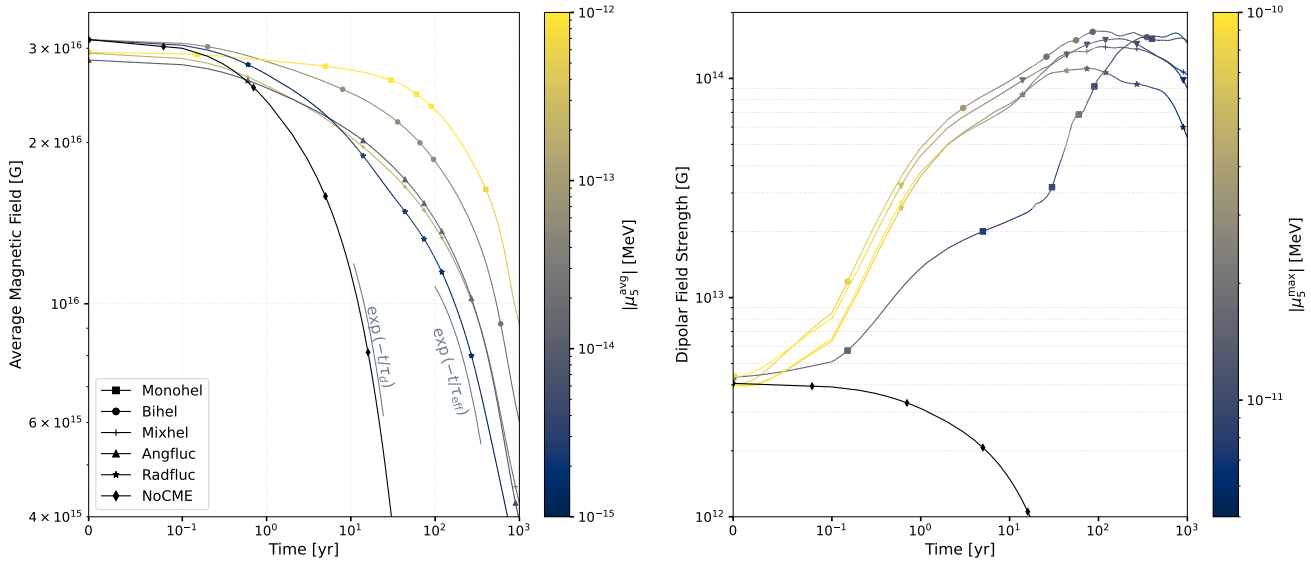

FIG. 6: Early-time evolution of the magnetic field for different simulation configurations over the first 10^3 years. The left panel shows the volume-averaged magnetic field, ranging from 4×10^{15} G to 3×10^{16} G, while the right panel shows the mean dipolar magnetic field, ranging from 10^{12} G to 2×10^{14} G. Simulation runs are represented by solid lines with distinct markers: squares indicate `Monohel` run, circles correspond to `Bihel` configuration, plus symbols denote `Mixhel` run, triangles represent `Angfluc` case, stars mark `Radfluc` run, and diamonds indicate the `NoCME` run. The colorbar in the left panel corresponds to the average chiral chemical potential, $\mu_5^{\rm avg}$, and the colorbar in the right panel corresponds to the maximum chiral chemical potential, $\mu_5^{\rm max}$. The `NoCME` run is shown in black, as it does not include the chirality effects.

CME—sourced by the magnetic field itself—primarily redistributes magnetic energy across spatial scales rather than amplifying the mean magnetic field, as illustrated in Fig. 5.

The decay of the mean magnetic field exhibits distinct slopes depending on the physical processes included in the simulations. In the `NoCME` case, where only Ohmic dissipation is considered, the magnetic field decays rapidly following an exponential law, $\propto \exp(-t/\tau_{\rm d})$, with an Ohmic timescale defined as $\tau_{\rm d} \equiv L^2/\eta \approx$ 20–25 yr. Here, L denotes a characteristic magnetic length scale, such as the radius of curvature of the magnetic field lines. All modes decay in the `NoCME` run, including the initially weak dipolar component, which decays more slowly owing to its smaller wavenumber; the corresponding results are summarized in Table I.

In contrast, in runs where the CME is active, the evolution deviates from the purely Ohmic case. In these simulations, the magnetic-field decay follows $\propto \exp(-t/\tau_{\rm eff})$, where the effective decay timescale is

$$\tau_{\rm eff} \approx \frac{\tau_d}{|1 - k_5 L|}. \tag{14}$$

This modified decay timescale reflects the competition between Ohmic dissipation and the chiral magnetic effect. $k_5 L < 1$ that slow down the dissipation (and that is what we mostly see). If $k_5 L = 1$, then the effective decay timescale diverges, meaning that we stop completely the dissipation, and if $k_5 L > 1$ ... The k_5 correction has a substantial dynamical impact and depends on both the sign and magnitude of the magnetic helicity. In particular, dissipation is enhanced when $k k_5 < 0$, reduced when $k k_5 > 0$, and can vanish altogether in the marginal case $k = k_5$ (this is a divergence actually).

We next examine the time evolution of the mean chiral chemical potential, $\mu_5^{\rm avg}$. In the figure we plot the absolute value of this quantity, since μ_5 can take either positive or negative values depending on the relative orientation of the electric field and the magnetic field. We find that the magnitude of the volume-averaged chiral chemical potential, $|\mu_5^{\rm avg}|$, is primarily determined by the initial magnetic-field configuration and remains nearly constant throughout the evolution. In the most favorable case—the `Monohel` run, $|\mu_5^{\rm avg}|$ reaches values of order 10^{-12} MeV, which is extremely small in the context of CME studies. In the `Bihel`, `Mixhel`, `Angfluc`, and `radfluc` runs the magnitude decreases to about $10^{-14} - 10^{-15}$ MeV, while it is identically zero in `NoCME` (see also Table I).

We find that the value of the $|\mu_5^{\rm avg}|$ determines the effective decay timescale of the mean magnetic field through the parameter k_5. Consequently, runs with larger values of $k_5^{\rm avg}$ exhibit slower magnetic-field decay. This explains why the helical run decays most slowly: it has the largest $k_5^{\rm avg}$ and therefore the smallest value of $|k - k_5|$, which leads to the largest $\tau_{\rm eff}$. A similar correspondence between the decay rate of the magnetic field and the initial value of $k_5^{\rm avg}$ is observed for the other runs.

In order of decreasing decay timescale, the runs follow the sequence: `Monohel`, `Bihel`, `Mixhel`, `Angfluc`, `Radfluc`, and finally `NoCME`, for which $k_5^{\rm avg} = 0$ and $\tau_{\rm eff} \equiv \tau_d$.

The time evolution of the dipolar magnetic field, shown in the left panel of Fig. 6, differs significantly among the various runs. In `NoCME`, no amplification of the dipolar component is observed, as the CME is inactive and therefore unable to redistribute magnetic energy across spatial scales. This behavior is consistent with the vanishing value of μ_5, indicated by the black curve. In contrast, all other simulations show a clear growth of the dipolar field, correlated with pronounced fluctuations in $\mu_5^{\rm max}$ (indicated by the colorbar).

As already reported in [1], three distinct stages characterize the evolution of the dipolar component. During the initial phase ($t \lesssim 0.1$ yr), the helical run exhibits only a marginal increase in the dipolar field, as the chiral asymmetry is still developing from the initially turbulent magnetic configuration. A similar early behavior is observed in the `Bihel` and `Mixhel` runs; however, in these cases the growth is more pronounced, which can be attributed to their larger values of $|\mu_5^{\rm max}|$. For the `Monohel` run, this initial stage is followed by a gradual growth phase lasting several decades, and subsequently by a second phase of exponential amplification extending over several more decades. We interpret this latter phase as the onset of the chiral magnetic instability (CMI), with the growth approximately following $\propto \exp(t/\tau_5)$, where

$$\tau_5 \equiv 1/(\eta k k_5^{\rm max}) \tag{15}$$

is driven by the maximum value of the chiral chemical potential $\mu_5^{\rm max}$. The field saturates at $B \gtrsim 10^{14}$ G after ~ 100 yr, in agreement with typical magnetar field strengths.

In `Bihel`, the exponential growth phase begins earlier and proceeds more rapidly, leading to saturation at $B \gtrsim 10^{14}$ G within only a few decades. In contrast, the mixed run initially follows a similar growth trend to the `Bihel` case, but saturates at an earlier time, around $B \approx 10^{14}$ G, and subsequently enters a decay phase that is faster than expected from standard Ohmic dissipation alone. This accelerated decay once the dipolar field reaches $\approx 10^{14}$ G, results from the CME actively destroying the large-scale field due to the anti-alignment of the electric current with the magnetic field. This mechanism will be discussed in more detail in the following section.

In contrast, the maximum value, $|\mu_5^{\rm max}|$, shows more pronounced temporal variations. Larger values of $|\mu_5^{\rm max}|$ indicate localized regions where the magnetic field is strongly helical, even though the net magnetic helicity remains close to zero. Since we plot the absolute value of $|\mu_5^{\rm max}|$, the presence of localized regions with positive helicity necessarily implies the existence of other regions with negative helicity, resulting in a nearly vanishing global helicity. We find that $|\mu_5^{\rm max}|$ reaches values of order 10^{-10} MeV at early times ($t \lesssim 1$ yr) in the runs with nearly zero net magnetic helicity, namely the `Bihel` and mixed runs. It then decreases to about 10^{-11} MeV after several decades of evolution. By contrast, in the helical run $|\mu_5^{\rm max}|$ remains lower, of order 10^{-11} MeV, and stays approximately constant over the entire simulated time span of a few centuries.

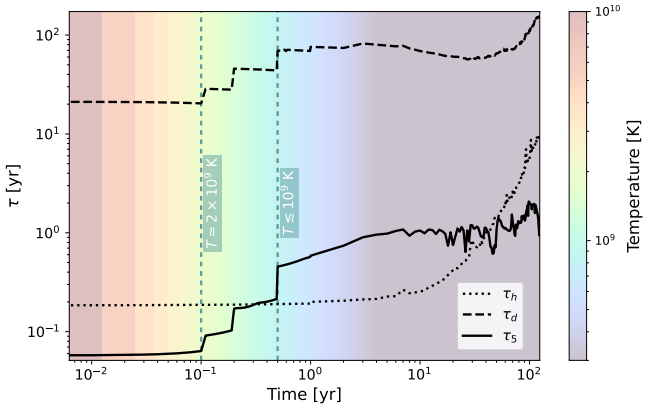

FIG. 7: Time evolution of the characteristic timescales in the neutron star crust. The dotted, dashed, and solid black curves correspond to the Hall (τ_h), Ohmic (τ_d), and chiral (τ_5) timescales, respectively. The color bar denotes the mean temperature evolution. Vertical green dashed lines indicate the epochs at which the temperature reaches $T \simeq 3 \times 10^9$ K and $T \simeq 10^9$ K.

C. Timescales

The characteristic timescales relevant to the interior of a neutron star crust are the Ohmic diffusion timescale, the chiral timescale, and the Hall drift timescale, defined as

$$\tau_d \equiv \frac{L^2}{\eta}, \qquad \tau_5 \equiv \frac{L}{\eta |k_5|}, \qquad \tau_h \equiv \frac{L^2}{f_h B_{\rm rms}}. \tag{16}$$

Here, L denotes a characteristic magnetic length scale, such as the radius of curvature of the magnetic field lines.

In the present simulations, the Hall term is neglected. This choice is motivated by two main considerations. First, our aim is to isolate and examine the effects of the CME for different magnetic field configurations and helicity content. This becomes challenging when both effects are included simultaneously, since in the presence of magnetic helicity the Hall term is expected to induce an inverse cascade [26], while the CME likewise generates an inverse-like cascade [1], both operating in the interior of a neutron star crust. Consequently, both mechanisms drive the transfer of magnetic energy from smaller to larger spatial scales, and their simultaneous inclusion would hinder a clear separation of their individual contributions. The second reason for neglecting the Hall term at this stage is of a numerical nature. Simulations that include both effects simultaneously require more advanced numerical techniques than those currently implemented

in the present version of the MATINS code. To our knowledge, simulations accounting for the combined action of the Hall term and the CME have not yet been explored in the literature.

To assess whether the Hall term could significantly influence our results, we examine the characteristic timescales relevant to the interior of a neutron star crust. These are the Ohmic diffusion timescale, the chiral timescale, and the Hall drift timescale, defined in Eq. (16). Figure 7 shows the temporal evolution of the characteristic timescales operating in the interior of a neutron star crust during the first 100 years of its evolution. The Hall timescale, τ_h, is represented by the dotted black line, the Ohmic diffusive timescale, τ_d, by the dashed black line, and the chiral timescale, τ_5, by the solid black line. The color bar indicates the cooling of the mean temperature value, while the vertical green dashed lines mark the epochs at which the temperature reaches approximately 2×10^9 K and 10^9 K, respectively. The results are presented for the Radfluc run.

During this early evolution, the neutron star undergoes thermal relaxation, during which the temperature decreases rapidly from $\sim 10^{10}$ K to $\sim 10^9$ K as the crust and core approach quasi-isothermal equilibrium [47]. This rapid temperature drop is reflected in the evolution of the magnetic diffusivity, which decreases as the star cools, and is consequently manifested in the Ohmic and chiral timescales, τ_d and τ_5, due to their dependence on η. The jumps observed in τ_d and τ_5 reflect variations in the magnetic diffusivity, which are most pronounced at early times and become progressively less significant as the star cools. These changes are computed self-consistently within the MATINS code. In contrast, the Hall timescale remains largely unaffected by the temperature evolution.

The Ohmic timescale is several orders of magnitude longer (slower) than both the Hall and chiral timescales. In contrast, the Hall and chiral timescales exhibit a strong interplay. During the first few months of the neutron star's evolution, the chiral timescale is shorter than the Hall timescale. As the star cools during thermal relaxation, there is a brief period ($t \approx 0.2$–0.5 yr) during which the two timescales become comparable. Subsequently, as cooling proceeds, the chiral timescale slows relative to the Hall timescale, which becomes faster by roughly a factor of two.

This behavior persists until the star reaches an age of approximately 30 years, at which point the Hall timescale increases significantly, whereas the chiral timescale remains nearly constant, with only a gradual increase due to the slow decrease of $k_5^{\max}$. The divergence between the timescales at this stage results from the CME transferring magnetic energy to larger scales, which causes the characteristic magnetic length scale L to increase rapidly. Since $\tau_h \propto L^2$ and $\tau_5 \propto L$, the growth of L impacts the Hall timescale more strongly, leading to its pronounced increase. The same effect also applies to the Ohmic timescale ($\tau_d \propto L^2$), which becomes progressively slower as L grows.

Finally, we note that in the present evolution, changes in the characteristic magnetic length scale L due to the Hall effect are not explicitly accounted for, which could alter the evolution of the timescales. It is also important to emphasize that the Hall timescale does not directly depend on whether the magnetic field is helical or non-helical; this information is instead encoded in the value of $k_5^{\max}$ and, consequently, in the chiral timescale. This distinction is crucial because, in regions where the CME is most effective, the magnetic field is aligned with the electric current (see Section II A). Therefore, in locally force-free regions, the Hall term is not expected to significantly affect the CME-driven evolution. A comprehensive assessment of both effects simultaneously is important and will be addressed in a follow-up study.

V. DISCUSSION

In the presence of a very strong magnetic field with $B \gtrsim B_{\rm QED}$, all electrons occupy the LLL and can move only along the direction of the magnetic field. As the magnetic helicity relaxes, an electric field is induced, resulting in a non-vanishing $\boldsymbol{E} \cdot \boldsymbol{B}$. Assuming $\boldsymbol{E} \cdot \boldsymbol{B} > 0$, a right-handed electron is converted into a left-handed electron by reversing the direction of its momentum. The left-handed electron then moves upward, outside of the LLL and this happens thanks to the chiral anomaly. Once electrons leave the LLL, they can flip chirality, thereby significantly reducing the chiral asymmetry. Nevertheless, this very small chiral asymmetry that is on the order of 10^{-11} MeV can induce significant variation in the magnetic field evolution, especially in transferring the magnetic energy between different spatial scales. This scenario has been proven very effective in the context of neutron star long-term evolution, in the presence of a helical magnetic field [1].

The helicity content of the magnetic field at neutron-star birth remains uncertain. If the chiral magnetic effect operates during core collapse, the initial chiral asymmetry can be converted into net magnetic helicity as the system relaxes toward chemical equilibrium [12]. In contrast, standard MHD scenarios preserve reflectional symmetry, so that an initially non-helical field develops mirror structures of opposite handedness, allowing magnetic energy to grow while the net helicity remains negligible [16–18].

Motivated by these uncertainties, we explore a range of plausible magnetic configurations representative of newborn neutron stars, in which the magnetic energy is predominantly concentrated at small scales, as expected from dynamo models. We systematically vary both the initial helicity content and its spatial distribution, thereby covering a broad spectrum of possible helicity configurations at birth. Within this framework, we investigate how different helicity configurations influence the development of the CME and, consequently, affect the long-term evolution of the magnetic field over

neutron-star timescales.

Both initially helical magnetic fields (e.g., the `Monohel` run) and non-helical configurations (i.e., the other setups described in Section III) are capable of triggering the CME, which subsequently drives the long-term evolution of the magnetic field. In all cases, we find that the CME can amplify the large-scale dipolar component from typical pulsar strengths of a few 10^{12} G up to magnetar-level fields of a few 10^{14} G within a century, provided that the instability develops on timescales shorter than Ohmic dissipation. Notably, non-helical configurations—such as the `Bihel` run, which is likely more representative of the magnetic field at birth—are found to be more efficient and faster in generating strong dipolar fields compared to initially helical configurations like `Monohel`. This behavior indicates that the onset of the chiral magnetic instability is primarily governed by the peak value of the chiral chemical potential, $\mu_5^{\rm max}$, rather than its volume-averaged value, $\mu_5^{\rm avg}$.

An additional key factor is the characteristic size of the regions carrying magnetic helicity. When the helicity fluctuates on very small spatial scales (i.e., $\lll 1\,$km), as in `Radfluc` setups, the associated chiral chemical potential varies rapidly between positive and negative values over short distances. In this regime, no coherent region with a sufficiently large $\mu_5^{\rm max}$ can develop to drive the instability. Instead, the rapid spatial oscillations effectively mimic a configuration with a nearly vanishing, spatially uniform μ_5, thereby suppressing the CME. This behavior is particularly evident in the `Radfluc` run, where helicity fluctuations occur on scales of $\sim 0.06\,$km within a crustal thickness of $\sim 0.86\,$km, leading to an effectively averaged-out chiral asymmetry. A similar effect is observed in the `Angfluc` run, although it is less pronounced due to the larger characteristic size of the helicity-carrying regions.

On the other hand, larger coherent regions of order $\sim 1\,$km—arguably a more realistic scenario (see also Reisenegger 52)—can sustain sufficiently large local values of μ_5 to trigger the CME. In such cases, the instability enables an efficient transfer of magnetic energy from small to large scales, ultimately leading to the formation of a stable, large-scale dipolar field.

These results point to a promising pathway for magnetar formation, in which a broad range of small-scale magnetic field configurations—whether initially helical or not—can give rise to strong, large-scale dipolar fields through the action of the CME. This implies that the CME should be systematically considered in studies of magnetic field evolution in neutron-star interiors, as its impact is self-regulated by the local conditions of the system. In particular, when the magnetic field is sufficiently strong and structured on small spatial scales such that the CMI develops on timescales shorter than Ohmic dissipation (see Fig. 7), efficient amplification toward large scales can occur, leading to magnetar formation. Conversely, when the resulting large-scale field is unstable and decays over time—as in the `Radfluc` and `Angfluc` cases—this may instead give rise to other classes of neutron stars, such as low-field magnetars or Central Compact Objects, which are characterized by strong but predominantly non-dipolar magnetic fields. By contrast, if the initial magnetic field is too weak, as is likely the case for typical rotation-powered pulsars, the CME is not efficiently triggered, thereby preventing any significant reorganization of magnetic energy toward large scales.

Finally, it is important to emphasize that future studies should incorporate additional physical processes, in particular studying the CME and the Hall effect simultaneously, in the evolution of the magnetic field. More importantly, a key missing ingredient is a systematic assessment of the magnetic helicity generated at birth. Proto-neutron star dynamo models have extensively studied the resulting magnetic field configurations, but the associated helicity has received little attention. Both the geometry and helicity established at birth are crucial, as the diversity of dynamo mechanisms can set the initial conditions that ultimately determine the neutron star's evolutionary pathway and observational class.

DATA AVAILABILITY

The source code used for the simulations of this study, the `MATINS` Code, is freely available on https://github.com/ice-csic-astroexotic/MATINS.

ACKNOWLEDGMENTS

CD is supported by the Ministerio de Ciencia, Innovación y Universidades (JDC2023-052227-I), co-funded by AEI (MCIN/AEI/10.13039/501100011033), the FSE+, and the Universidad de Alicante, and also acknowledges support from the Conselleria d'Educació, Cultura, Universitats i Ocupació de la Generalitat Valenciana (grant CIPROM/2022/13) and the AEI grant PID2021-127495NB-I00.

Appendix A: Initial magnetic field and helicity distribution

To define the initial magnetic field configurations described in Section III, we decompose the magnetic field into poloidal ($\boldsymbol{B}_p$) and toroidal ($\boldsymbol{B}_t$) components [53]:

$$\boldsymbol{B} = \boldsymbol{B}_p + \boldsymbol{B}_t, \tag{A1}$$

$$\begin{aligned} \boldsymbol{B}_t &= -\boldsymbol{r}\times\boldsymbol{\nabla}\Psi, \qquad \boldsymbol{A}_t = -\boldsymbol{r}\times\boldsymbol{\nabla}\Phi, \\ \boldsymbol{B}_p &= \boldsymbol{\nabla}\times\boldsymbol{A}_t = -\boldsymbol{r}\Delta\Phi + \boldsymbol{\nabla}\frac{\partial}{\partial r}\left(r\Phi\right), \end{aligned} \tag{A2}$$

where $\boldsymbol{A}_t$ is the toroidal vector potential. The two scalar functions $\Phi(\boldsymbol{r},t)$ and $\Psi(\boldsymbol{r},t)$ uniquely define the poloidal

and toroidal components, respectively. Next, we expand the scalar functions in spherical harmonics [54]:

$$\Phi(t,r,\theta,\phi) = \frac{1}{r}\sum_{\ell m}\Phi_{\ell m}(r,t)Y_{\ell m}(\theta,\phi),$$
$$\Psi(t,r,\theta,\phi) = \frac{1}{r}\sum_{\ell m}\Psi_{\ell m}(r,t)Y_{\ell m}(\theta,\phi), \quad \text{(A3)}$$

where $\ell = 1, 2, \ldots$ denotes the multipole degree and $m = -\ell, \ldots, \ell$ the azimuthal order.

We define the radial poloidal scalar function, $\Phi(\boldsymbol{r}, t{=}0)$, as:

$$\Phi_{\ell m}(r) = \Phi^0_{\ell m}\, k_r\, r\, (a + \tan(k_r R)\, b), \quad \text{(A4)}$$

where the coefficients a and b are chosen to satisfy the inner and outer boundary conditions [55], and $\Phi^0_{\ell m}$ is the normalization factor for the poloidal function. The radial wavenumber k_r is taken in the range $k_r \approx 400$–$450\,\mathrm{km}^{-1}$, chosen to balance the fastest-growing CME modes against Ohmic dissipation (see also Fig. 3 of [1]). This parameter is particularly important in the radial direction, where both Ohmic dissipation and the CME are highly sensitive to microphysical properties that vary significantly with density.

The normalized coefficients $\Phi^0_{\ell m}$ and $\Psi^0_{\ell m}$ set the relative amplitudes and phases of the poloidal and toroidal components for a given ℓ and m, thereby controlling the distribution of magnetic energy across spatial scales. Together with the relative phases, they influence the local sign and spatial pattern of the magnetic helicity, which also affects the characteristic size of magnetic helicity structures. For helical configurations (e.g., the `Monohel` run), the poloidal and toroidal components are intrinsically linked by construction [26]. Accordingly, we define the radial toroidal scalar function, $\Psi(r, t{=}0)$, as

$$\Psi_{\ell m}(r) = \alpha_{\ell m}\, \Phi_{\ell m}(r), \quad \text{(A5)}$$

where, for a conservative choice, we adopt $\alpha_{\ell m} = \sqrt{\ell(\ell+1)}/R$, with R denoting the radius at the surface of the computational domain. For a maximally helical configuration, one would instead set $\alpha_{\ell m} = k$. In the `Monohel` run, $\Psi^0_{\ell m}$ is equal to $\Phi^0_{\ell m}$.

To avoid imposing an initial net magnetic helicity by construction, we define the normalized poloidal and toroidal coefficients, $\Phi^0_{\ell m}$ and $\Psi^0_{\ell m}$, independently—i.e., without introducing correlations between them—for the `Bihel`, `Mixhel`, and `Angfluc` runs. We also ensure that the characteristic size of magnetic helicity structures decreases in the angular direction across these runs. In the `Bihel` run, opposite signs of magnetic helicity are enforced between the northern and southern hemispheres, producing mirror-symmetric structures that cancel out globally, yielding negligible net helicity. In `Mixhel` and `Angfluc` simulations, the local helicity varies randomly between positive and negative, resulting in configurations with negligible net helicity (as illustrated in Fig. 3).

For the `Radfluc` run, we adopt the same $\Phi^0_{\ell m}$ and $\Psi^0_{\ell m}$ as in the `Bihel` run, but assign different radial wavenumbers to the poloidal and toroidal scalar functions, with $k_r^{\rm pol} \approx 400$ and $k_r^{\rm tor} \approx 450$. This produces small-scale, localized helicity fluctuations in the radial direction while maintaining an approximately vanishing net helicity. Fig. 8 shows the meridional profile of the normalized local magnetic helicity, $\chi(r, \theta, \phi, t_0)$, in the angular interval $65° \le \theta \le 115°$, highlighting the strong spatial fluctuations of magnetic helicity across the crustal layers.

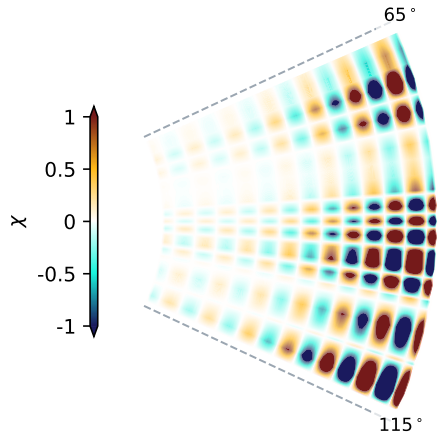

FIG. 8: Meridional profile of the normalized magnetic helicity for the Fluctuations runs in the angular interval $65° \le \theta \le 115°$. The crust is radially magnified by a factor of 8 for improved visualization.

Finally, we employ the curl operators adapted to cubed-sphere coordinates [45] and derive the magnetic field components from the poloidal and toroidal scalar functions using Eq. (A2). This approach guarantees an initial magnetic field that is divergence-free (to machine precision), free of axis singularities, and intrinsically helical—a crucial property for studying CME-driven magnetic evolution.

[1] C. Dehman and J. A. Pons, Phys. Rev. Res. **7**, 033231 (2025).
[2] N. R. Poniatowski, American Journal of Physics **87**, 436–443 (2019).
[3] S. L. Adler, Physical Review **177**, 2426 (1969).
[4] J. S. Bell and R. Jackiw, Nuovo Cimento A Serie **60**, 47 (1969).
[5] D. S. Freed, arXiv e-prints , arXiv:2107.03557 (2021),

arXiv:2107.03557 [math.HO].
[6] A. Boyarsky, J. Fröhlich, and O. Ruchayskiy, Phys. Rev. Lett. **108**, 031301 (2012), arXiv:1109.3350 [astro-ph.CO].
[7] S. A. Balbus and J. F. Hawley, Astrophys. J. **376**, 214 (1991).
[8] M. Obergaulinger, H. T. Janka, and M. A. Aloy, MNRAS **445**, 3169 (2014), arXiv:1405.7466 [astro-ph.SR].
[9] M. Á. Aloy and M. Obergaulinger, MNRAS **500**, 4365 (2021), arXiv:2008.03779 [astro-ph.HE].
[10] A. Reboul-Salze, J. Guilet, R. Raynaud, and M. Bugli, A&A **645**, A109 (2021), arXiv:2005.03567 [astro-ph.HE].
[11] Y. Masada, T. Takiwaki, and K. Kotake, Astrophys. J. **924**, 75 (2022), arXiv:2001.08452 [astro-ph.HE].
[12] J. Matsumoto, N. Yamamoto, and D.-L. Yang, prd **105**, 123029 (2022), arXiv:2202.09205 [astro-ph.HE].
[13] P. Barrère, J. Guilet, R. Raynaud, and A. Reboul-Salze, A&A **695**, A183 (2025), arXiv:2407.01775 [astro-ph.HE].
[14] C. Dehman, D. Viganò, S. Ascenzi, J. A. Pons, and N. Rea, MNRAS **523**, 5198 (2023), arXiv:2305.06342 [astro-ph.HE].
[15] A. Igoshev, P. Barrère, R. Raynaud, J. Guilet, T. Wood, and R. Hollerbach, Nature Astronomy **9**, 541 (2025), arXiv:2501.04768 [astro-ph.HE].
[16] L. Woltjer, Proceedings of the National Academy of Sciences **44**, 489 (1958), https://www.pnas.org/doi/pdf/10.1073/pnas.44.6.489.
[17] J. B. Taylor, Phys. Rev. Lett. **33**, 1139 (1974).
[18] G. Bodo, F. Cattaneo, A. Mignone, and P. Rossi, The Astrophysical Journal **843**, 86 (2017).
[19] A. Brandenburg and K. Subramanian, Physics Reports **417**, 1 (2005).
[20] H. K. Moffatt, Journal of Fluid Mechanics **35**, 117 (1969).
[21] M. A. Berger and G. B. Field, Journal of Fluid Mechanics **147**, 133 (1984).
[22] V. I. Arnol'd and B. A. Khesin, Annual Review of Fluid Mechanics **24**, 145 (1992).
[23] A. A. Pevtsov, M. A. Berger, A. Nindos, A. A. Norton, and L. van Driel-Gesztelyi, Space Sci. Rev., **186**, 285 (2014).
[24] E. Pariat, G. Valori, P. Démoulin, and K. Dalmasse, A&A **580**, A128 (2015), arXiv:1506.09013 [astro-ph.SR].
[25] A. Brandenburg, Astrophys. J. **901**, 18 (2020), arXiv:2006.12984 [astro-ph.HE].
[26] C. Dehman and A. Brandenburg, A&A **694**, A39 (2025), arXiv:2408.08819 [astro-ph.HE].
[27] D. Biskamp, *Nonlinear Magnetohydrodynamics*, Cambridge Monographs on Plasma Physics (Cambridge University Press, 1997).
[28] S. B. Treiman, R. Jackiw, B. Zumino, and E. Witten, *Current Algebra and Anomalies* (Princeton University Press, 1985).
[29] K. Kamada, N. Yamamoto, and D.-L. Yang, Progress in Particle and Nuclear Physics **129**, 104016 (2023).
[30] D. Grabowska, D. B. Kaplan, and S. Reddy, prd **91**, 085035 (2015), arXiv:1409.3602 [hep-ph].
[31] G. Sigl and N. Leite, jcap **2016**, 025 (2016), arXiv:1507.04983 [astro-ph.HE].
[32] D. B. Kaplan, S. Reddy, and S. Sen, prd **96**, 016008 (2017), arXiv:1612.00032 [hep-ph].
[33] I. Rogachevskii, O. Ruchayskiy, A. Boyarsky, J. Fröhlich, N. Kleeorin, A. Brandenburg, and J. Schober, apj **846**, 153 (2017), arXiv:1705.00378 [physics.plasm-ph].
[34] A. Vilenkin, Phys. Rev. D **22**, 3080 (1980).
[35] P. J. Feibelman, Phys. Rev. D **4**, 1589 (1971).
[36] M. A. Alpar, S. A. Langer, and J. A. Sauls, Astrophys. J. **282**, 533 (1984).
[37] J. A. Pons and U. Geppert, A&A **470**, 303 (2007), arXiv:astro-ph/0703267 [astro-ph].
[38] J. A. Pons, C. Dehman, and D. Viganò, arXiv e-prints , arXiv:2509.06699 (2025), arXiv:2509.06699 [astro-ph.HE].
[39] A. Kostenko and C. Thompson, The Astrophysical Journal **869**, 44 (2018).
[40] C. Thompson and A. Kostenko, The Astrophysical Journal **904**, 184 (2020).
[41] L. D. Landau and E. M. Lifshits, *Quantum Mechanics: Non-Relativistic Theory*, Course of Theoretical Physics, Vol. v.3 (Butterworth-Heinemann, Oxford, 1991).
[42] V. A. Miransky and I. A. Shovkovy, Phys. Rep. **576**, 1 (2015), arXiv:1503.00732 [hep-ph].
[43] D. E. Kharzeev, L. D. McLerran, and H. J. Warringa, Nuclear Physics A **803**, 227 (2008).
[44] N. P. Armitage, E. J. Mele, and A. Vishwanath, Reviews of Modern Physics **90**, 015001 (2018), arXiv:1705.01111 [cond-mat.str-el].
[45] C. Dehman, D. Viganò, J. A. Pons, and N. Rea, MNRAS **518**, 1222 (2023), arXiv:2209.12920 [astro-ph.HE].
[46] S. Ascenzi, D. Viganò, C. Dehman, J. A. Pons, N. Rea, and R. Perna, arXiv e-prints , arXiv:2401.15711 (2024), arXiv:2401.15711 [astro-ph.HE].
[47] A. Y. Potekhin, J. A. Pons, and D. Page, Space Science Reviews **191**, 239 (2015).
[48] J. M. Pearson, N. Chamel, A. Y. Potekhin, A. F. Fantina, C. Ducoin, A. K. Dutta, and S. Goriely, Monthly Notices of the Royal Astronomical Society **481**, 2994 (2018), https://academic.oup.com/mnras/article-pdf/481/3/2994/25817956/sty2413.pdf.
[49] R. Raynaud, J. Guilet, H.-T. Janka, and T. Gastine, Science Advances **6**, eaay2732 (2020), arXiv:2003.06662 [astro-ph.HE].
[50] R. Durrer and C. Caprini, JCAP **2003**, 010 (2003).
[51] P. Esposito, N. Rea, A. Borghese, F. C. Zelati, D. Viganò, G. L. Israel, A. Tiengo, A. Ridolfi, A. Possenti, M. Burgay, D. Götz, F. Pintore, L. Stella, C. Dehman, M. Ronchi, S. Campana, A. Garcia-Garcia, V. Graber, S. Mereghetti, R. Perna, G. A. R. Castillo, R. Turolla, and S. Zane, The Astrophysical Journal Letters **896**, L30 (2020).
[52] A. Reisenegger, A&A **499**, 557 (2009), arXiv:0809.0361 [astro-ph].
[53] S. Chandrasekhar and P. C. Kendall, Astrophys. J. **126**, 457 (1957).
[54] F. Krause and K.-H. Rädler, *Oxford: Pergamon Press, 1980* (Pergamon Press, Oxford, 1980).
[55] D. N. Aguilera, J. A. Pons, and J. A. Miralles, A&A **486**, 255 (2008), arXiv:0710.0854 [astro-ph].